Pergamon

Int. J. Heat Mass Transfer. Vol. 41, No. 17, pp. 2573–2580, 1998

Printed in Great Britain
0017–9310/98 $19.00 + 0.00

PII: S0017-9310(97)00374-8

Flow and heat transfer in convection-dominated melting in a rectangular cavity heated from below

ZHEN-XIANG GONG and ARUN S. MUJUMDAR†
Department of Chemical Engineering, McGill University, Montreal, Canada H3A 2A7

(*Received* 11 *April* 1997 *and in final form* 20 *November* 1997)

Abstract—Melting of a pure phase change material (PCM) in a rectangular container heated from below is simulated using the Streamline Upwind/Petrov Galerkin finite element method in combination with a fixed grid primitive variable method. Boussinesq assumption is invoked and two-dimensionality is assumed. Flow patterns for a wide range of Rayleigh numbers are presented. Instability of free convection flow during the melting process is discovered and discussed. © 1998 Elsevier Science Ltd. All rights reserved.

1. INTRODUCTION

Although many experimental and numerical studies have been dedicated to convection-dominated melting of phase change materials (PCMs) for various geometry configurations, e.g., along a vertical wall, inside as well as around a horizontal cylinder, etc., little effort has been reported on the melting of a PCM heated from below.

Yen and Galea [1, 2] and Seki *et al.* [3] experimentally studied the melting of a horizontal ice slab heated from below. Hale and Viskanta [4] performed experiments for melting from below and solidification from top of *n*-octadecane in a rectangular cavity. They did not present flow patterns and phase change interface shapes, however, Gau *et al.* [5] presented flow visualization for melting from below of a *n*-octadecane slab in a rectangular cavity. Diaz and Viskanta [6] extended the experiments of Gau *et al.* [5] to morphology observation of the liquid/solid interface.

In this paper the melting of a pure PCM in a rectangular container heated from below is simulated with the Streamline Upwind/Petrov Galerkin finite element in combination with a fixed grid primitive variable method. The Boussinesq assumption is invoked and two-dimensionality is assumed. Different flow patterns are obtained for different Rayleigh numbers. Instability of free convection flow is discovered. Sample results are presented and discussed.

2. MATHEMATICAL FORMULATION

For the mathematical description of a melting or freezing process the following assumptions are made: (1) heat transfer in the PCM is conduction/convection controlled, and the melt is Newtonian and incompressible; (2) the flow in the melt is laminar and viscous dissipation is negligible; (3) the densities of the solid and liquid are equal; (4) the Boussinesq assumption is valid for free convection, i.e. density variations are considered only insofar as they contribute to buoyancy, but are otherwise neglected; (5) the solid PCM is fixed to the container wall during the melting process.

Based on the above assumptions and following the enthalpy-porosity model [7, 8], the governing equations in tensor form are

$$u_{i,i} = 0 \tag{1}$$

$$\rho\left(\frac{\partial u_i}{\partial t} + u_j u_{i,j}\right) = -p_{,i} + [\mu(u_{i,j} + u_{j,i})]_{,j} - \rho g_i \beta (T - T_0) + A u_i \tag{2}$$

$$\rho\left(\frac{\partial h}{\partial t} + u_j T_{,j}\right) = (kT_{,j})_{,j}. \tag{3}$$

In equation (2)

$$A = -C(1-\lambda)^2/(\lambda^3 + b) \tag{4}$$

in which b is a small constant introduced to avoid division by zero and C is a constant accounting for the morphology of the mushy region. In general b is assigned a value of 0.001. For isothermal phase change (pure PCM) C is assigned a value of 1.6×10^6.

The initial and boundary conditions are

initial conditions

$$T(x,0) = T^0(x)$$
$$u_i(x,0) = u_i^0(x) \tag{5}$$

boundary conditions

$$u_i = \bar{u}_i(s,t) \quad \text{on } \Gamma_u$$
$$T = \bar{T}(s,t) \quad \text{on } \Gamma_T$$
$$q = -(kT_{,j})n_j(s) = q_a(s,t) + q_c(s) + q_r(s) \quad \text{on } \Gamma_q. \tag{6}$$

† Author to whom correspondence should be addressed.

NOMENCLATURE

A	porosity function for the momentum equation
A^*	dimensionless form of A
b	a small constant
c	specific heat
C	constant
Fo	Fourier number
g_i	gravitational force vector
h	enthalpy
H	dimensionless enthalpy
k	heat conductivity
L_e	effective melt height
L_x	length of rectnagular enclosure in x direction
L_y	length of rectangular enclosure in y direction
$\mathbf{n}_i$	surface unit normal vector
p	fluid pressure
P	dimensionless fluid pressure
Pr	Prandtl number
q	heat flux
q_a	prescribed heat flux
q_c	convective heat flux
q_r	radiative heat flux
Ra	Rayleigh number
s	boundary surface coordinate
Ste	Stefan number
t	time
T	temperature
T_0	reference temperature
T_m	melting point of PCM
T_w	isothermal wall temperature
u_x	velocity in x direction
u_y	velocity in y direction
u_i	velocity component
U	dimensionless velocity of x direction
V	dimensionless velocity of y direction
x, y	coordinate
X, Y	dimensionless coordinate.

Greek symbols

α	diffusivity
β	expansion coefficient
γ	penalty parameter
Γ	boundary
Δh	latent heat
Δt	time step
θ	dimensionless temperature
λ	porosity of a mush zone
μ	viscosity
ρ	density
ω	the angle of horizontal direction to x axis.

Subscripts

l	liquid
s	solid
x	component of x direction
y	component of y.

Superscript

$\bar{}$	overbar, boundary value of the variable
0	initial value.

In this study the penalty formulation [9, 10] is employed to treat the incompressibility constraint. According to the penalty formulation, the continuity equation is replaced by

$$u_{i,i} = -\frac{1}{\gamma}p \tag{7}$$

where γ is the penalty parameter which is generally assigned a value of 1.0×10^9.

Substitution of equation (7) into equation (2) yields

$$\rho\left(\frac{\partial u_i}{\partial t} + u_j u_{i,j}\right)$$

$$= \frac{1}{\gamma}(u_{i,i})_{,i}[\mu(u_{i,j}+u_{j,i})]_{,j} - \rho g_i \beta(T - T_0) + A u_i. \tag{8}$$

The mass conservation equation is eliminated from the system of equations to be solved because of the utilization of the penalty formulation.

Once the velocity and temperature fields are known, the pressure filed is calculated *a posteriori* if desired at any step by solving the Poisson equation [11]

$$-(p_{,j})_{,j} = \rho(u_j u_{i,j})_{,i} + \rho\beta(g_j T_{,j}) \tag{9}$$

subject to homogeneous Neumann conditions along the boundary Γ, i.e.

$$n_j p_{,j} = 0. \tag{10}$$

In order to obtain a unique pressure field it is necessary to set the pressure at one point in the domain equal to a reference pressure.

The Streamline Upwind/Petrov Galerkin finite element method [10–12] is utilized to solve the governing equations. A source-based method [13, 14] is employed to treat the latent heat effect. For detailed information of the numerical model please see Gong and Mujumdar [15].

3. DIMENSIONLESS FORM OF THE GOVERNING EQUATIONS

Non-dimensionalization of the governing equations (1)–(3) yield the dimensionless governing equations for two-dimensional problems subjected to the Dirichlet boundary condition as follows:

Solid region:

$$\frac{\partial H}{\partial Fo}=\frac{k_s}{k_l}Ste\left(\frac{\partial^2\theta}{\partial X^2}+\frac{\partial^2\theta}{\partial Y^2}\right). \tag{11}$$

Liquid region:

$$\frac{\partial U}{\partial X}+\frac{\partial V}{\partial Y}=0 \tag{12}$$

$$\frac{\partial U}{\partial Fo}+U\frac{\partial U}{\partial X}+V\frac{\partial U}{\partial Y}=-\frac{\partial P}{\partial X}+Pr\left(\frac{\partial^2 U}{\partial X^2}+\frac{\partial^2 U}{\partial Y^2}\right)+Ra\,Pr\sin\omega+A^*U \tag{13}$$

$$\frac{\partial V}{\partial Fo}+U\frac{\partial V}{\partial X}+V\frac{\partial V}{\partial Y}=-\frac{\partial P}{\partial Y}+Pr\left(\frac{\partial^2 V}{\partial X^2}+\frac{\partial^2 V}{\partial Y^2}\right)+Ra\,Pr\cos\omega+A^*V \tag{14}$$

$$\frac{\partial H}{\partial Fo}+U\frac{\partial H}{\partial X}+V\frac{\partial H}{\partial Y}=Ste\left(\frac{\partial^2\theta}{\partial X^2}+\frac{\partial^2\theta}{\partial Y^2}\right) \tag{15}$$

in which

$$\begin{cases} H=\dfrac{c_s}{c_l}Ste\,\theta, & \theta<0 \\ H=Ste\,\theta+1 & \theta>0 \end{cases} \tag{16}$$

and

$$U=\frac{u_xL_y}{\alpha_l},\quad V=\frac{u_yL_y}{\alpha_l},\quad \theta=\frac{T-T_m}{T_w-T_m},$$

$$H=\frac{h-c_sT_m}{\Delta h},\quad P=\frac{pL_y^2}{\rho\alpha_l^2}\quad X=\frac{x}{L_y},\quad Y=\frac{y}{L_y},$$

$$A^*=\frac{AL_y^2}{\rho\alpha_l},\quad Fo=\frac{t\alpha_l}{L_y^2},\quad Pr=\frac{c_l\mu}{k_l}$$

$$Ra=\frac{\rho^2c_lg\beta L_y^3(T_w-T_m)}{\mu k_l},\quad Ste=\frac{c_l(T_w-T_m)}{\Delta h}. \tag{17}$$

It is obvious that a melting or solidification process is governed by the following five dimensionless parameters, Rayleigh number (Ra), Prandtl number (Pr), Stefan number (Ste), the ratios of solid/liquid specific heat (c_s/c_l) and heat conductivity (k_s/k_l).

It should be noted that for melting from below the Rayleigh number (Ra) in eqn (17) defined based on the container height, L_y, is not the true Rayleigh number. The true Rayleigh number should be calculated using the actual melt height (L_e) instead of the height of the cavity (L_y). Since the melt height (L_e) is time-dependent, the true Rayleigh number also varies with time during the melting process.

4. TEST OF THE NUMERICAL MODEL

The above mentioned numerical model is compared with the experimental results of Gau and Viskanta [16] and the implicit finite difference results of Lacroix [17] for the melting of a pure metal (gallium) inside a two-dimensional rectangular cavity (height $L_y = 0.0445$ m; width $L_x = 0.089$ m). The gallium is assumed to be initially at its fusion temperature. The top and bottom boundaries are adiabatic. At time $t = 0$, the temperature of the left vertical wall is suddenly raised to a prescribed temperature above the melting point. The values of the governing dimensionless numbers and aspect ratio used in the numerical experiments are listed in Table 1.

Figure 1 compares the predicted phase front with both the experimental results of Gau and Viskanta [16] and the finite difference predictions of Lacroix [17]. It is seen from this figure that the present model is in good agreement with the results of the above-mentioned references.

The discrepancy between the predicted phase front of the present model and the experimental results is due to two possible reasons. First, in the experiment, the solid showed an initial subcooling of approximately 2°C. This degree of subcooling is significant in light of the fact that the heated wall was only 8°C higher than the melting temperature of gallium. The second reason is that it is difficult to impulsively heat the vertical wall to a desired temperature because of its finite thermal inertia. The discrepancy of predicted phase front between the present model and Lacroix's

Table 1. Parameters used in the test runs for accuracy

R	Aspect ratio L_y/L_x	0.5
Ra	Rayleigh number	2.2×10^5
Pr	Prandtl number	0.021
Ste	Stefan number	0.042
c_s/c_l	Ratio of solid/liquid specific heat	1
k_s/k_l	Ratio of solid/liquid heat conductivity	1

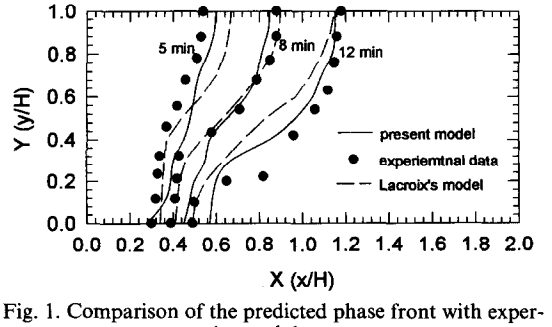

Fig. 1. Comparison of the predicted phase front with experimental data.

model is probably due to the differences in the numerical methods used. Lacroix used a front tracking method while this model uses a fixed-grid enthalpy-porosity approach to model the phase change effects.

5. RESULTS AND DISCUSSION

Using the above-described numerical model simulation runs were carried out for melting of a PCM in a rectangular cavity heated from below. The top and the two vertical walls are assumed to be adiabatic (see Fig. 2). The parameters for the computed problem are listed in Table 2. The phase change material used is *n*-octadecane (99% pure).

Grid-dependence experiments indicated that the maximum difference of the temperature at an identical location is within 0.16% between using 20×20 elements with a dimensionless time step of 4.32×10^{-5} and 30×30 elements with the same time step; while the difference is only 0.07% between using 30×30 elements with a dimensionless time step of 4.32×10^{-5} and 40×40 elements with a time step of 2.16×10^{-5}. Therefore, 30×30 elements with a time step of 4.32×10^{-5} were used for this and all the subsequent computations considering both accuracy and computing time.

It is known from experiments that three-dimensional convection cells develop and last for a short period of time during the early stage in two-dimensional melting of a PCM heated from below [5]. In this study we neglect three-dimensional convection since we employ a two-dimensional model. However, the duration of the three-dimensional convection is very short [1, 5] compared with the whole melting process so that the two-dimensional results may be close to reality. No experimental data are available for direct validation at this time.

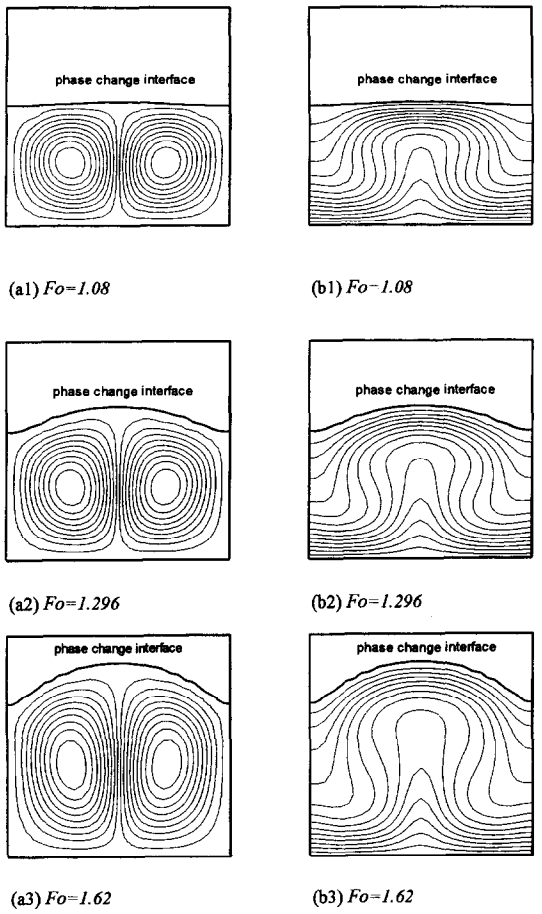

Fig. 3. Streamlines and isotherms in the melt zone for heating from below ($Ra = 2.844 \times 10^4$).

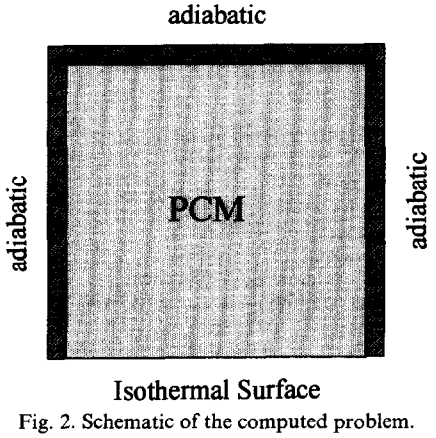

Fig. 2. Schematic of the computed problem.

Table 2. Parameters used in the simulation runs

R	Aspect ratio L_y/L_x	1.0
Ra	Rayleigh number	2.844×10^6
Pr	Prandtl number	46.1
Ste	Stefan number	0.138
c_s/c_l	Ratio of solid/liquid specific heat	0.964
k_s/k_l	Ratio of solid/liquid heat conductivity	2.419
θ_i	Initial dimensionless temperature	−0.0256

Figure 3 shows the computed streamlines and isotherms at different Fo values for $Ra = 2.844 \times 10^4$. From these figures it is seen that free convection does not develop until over half of the PCM is melted. Why does convection develop so late? As mentioned earlier, the actual Rayleigh number for melting from below is varying (increasing) with the melting process. The earlier the melting process, the smaller the melt height, the smaller the true current Rayleigh number. Under a small Rayleigh number free convection effects are small.

For $Ra = 2.844 \times 10^4$ two convection cells develop during the melting process. These two convection cells are symmetric. The number of convection cells is time-independent. Due to the convection circulation flow, the phase change interface is not flat. Since the flow direction of the left convection cell is anti-clockwise and that of the right cell is clockwise, the melt is heated

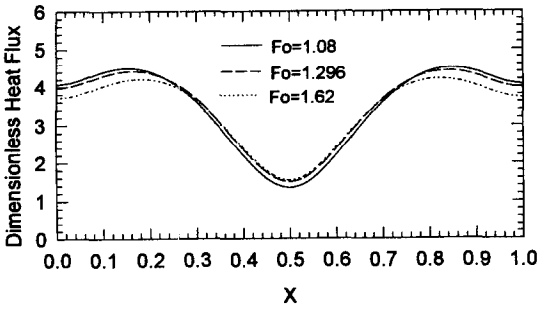

Fig. 4. Local dimensionless heat flux distribution along the heated surface at different Fo values ($Ra = 2.844 \times 10^4$).

to the highest temperature at bottom center and then floats up, reaches the phase change interface and splits into opposite directions. The melt is cooled as it flows through the phase change interface. This explains why the phase change interface has a peak at the center.

Figure 4 displays the local dimensionless heat flux distribution curves corresponding to the flow patterns in Fig. 3. According to the dimensionless energy equation [equation (15)] the dimensionless heat flux in liquid phase is $\partial\theta/\partial X$. From this figure one can see that there is a trough at the center of the heat flux curve. This trough corresponds to the junction of the two convection cells in Fig. 3. It is well known the lower the temperature difference the lower the heat flux. Since the melt temperature is the highest at the bottom center (see the isotherms in Fig. 3) and the bottom wall is isothermal, the temperature difference is the lowest at the bottom center. As a result, the heat flux is the lowest there.

Figure 5 presents the predicted streamlines and isotherms at different Fo values for $Ra = 2.844 \times 10^5$. Unlike the case of $Ra = 2.844 \times 10^4$, free convection develops much earlier in the case of $Ra = 2.844 \times 10^5$. Also four symmetric convection cells persist during the whole melting process at this Rayleigh number. As in the case of $Ra = 2.844 \times 10^4$ the number of convection cells is also time-independent. Due to the effects of the four convection cells two symmetric cusps on the liquid/solid phase change interface form. The left cusp corresponds to the junction of the left two convection cells. This cusp forms because the flow direction of the leftmost convection cell is clockwise and that of its neighbour is anti-clockwise. Due to this fact the melt temperature at the junction of the two cells on the phase change interface is the lowest [see the corresponding isotherms in (b1)–(b4)]. This explains why the phase change interface at this location is the lowest.

Figure 6 shows the local dimensionless heat flux distribution curves at different Fo values corresponding to the streamline patterns shown in Fig. 5. From this figure it is seen that there are two crests and one trough at the center on the heat flux distribution curves. The left crest corresponds to the junction of the two leftmost convection cells and the

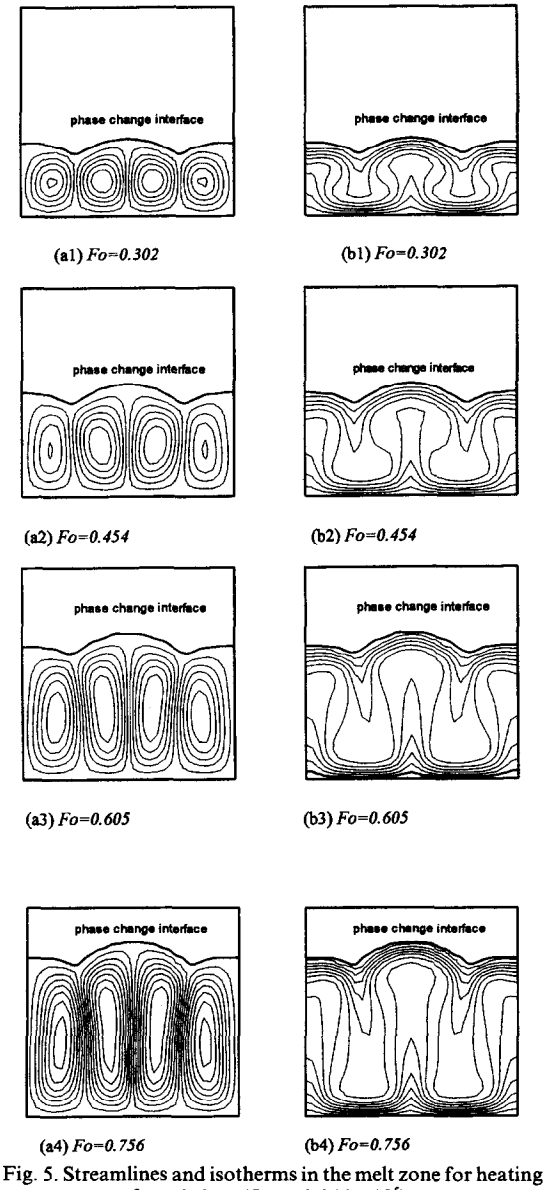

Fig. 5. Streamlines and isotherms in the melt zone for heating from below ($Ra = 2.844 \times 10^5$).

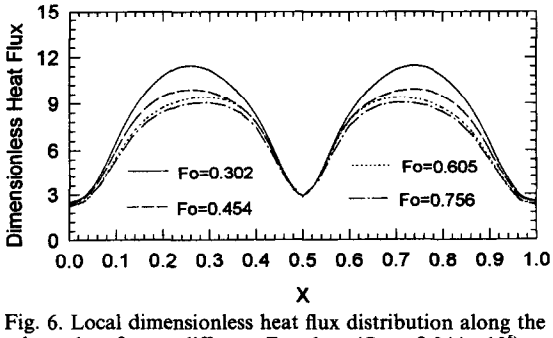

Fig. 6. Local dimensionless heat flux distribution along the heated surface at different Fo values ($Ra = 2.844 \times 10^5$).

trough corresponds to the junction of the second and third convection cells from the left. Due to the symmetry of the convection cells the heat flux distribution is also symmetric.

Figure 7 shows the predicted streamlines and isotherms at different Fo values for $Ra = 2.844 \times 10^6$.

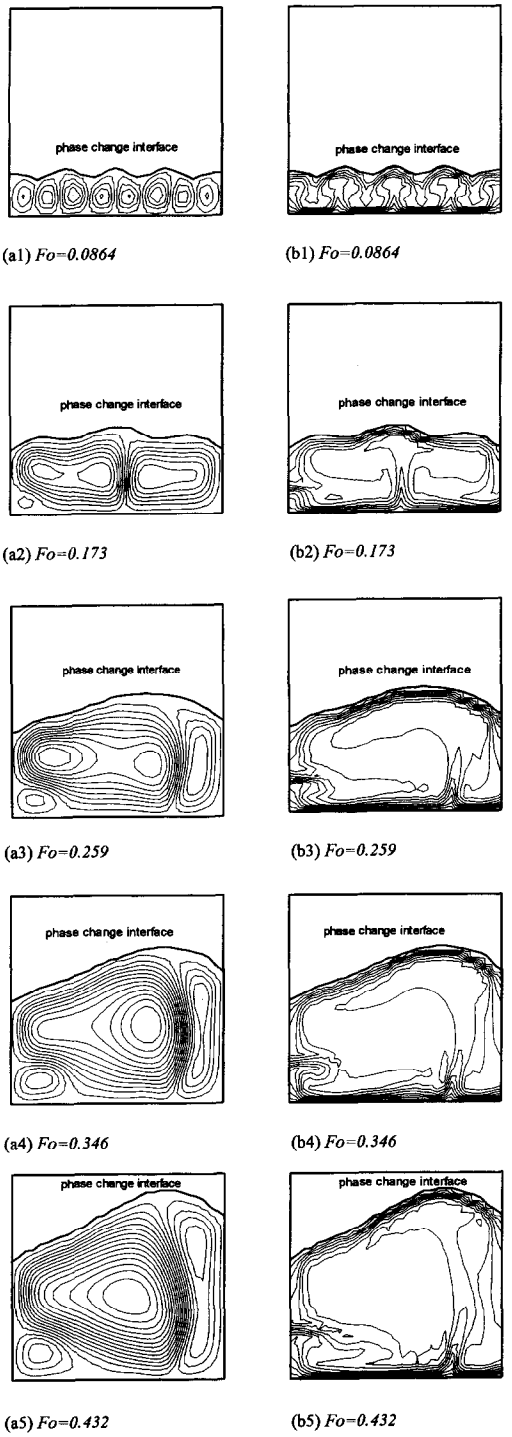

(a1) *Fo=0.0864* (b1) *Fo=0.0864*

(a2) *Fo=0.173* (b2) *Fo=0.173*

(a3) *Fo=0.259* (b3) *Fo=0.259*

(a4) *Fo=0.346* (b4) *Fo=0.346*

(a5) *Fo=0.432* (b5) *Fo=0.432*

Fig. 7. Streamlines and isotherms in the melt zone for heating from below ($Ra = 2.844 \times 10^6$).

From these streamline patterns it is seen that at $Fo = 0.0864$ a total of eight convection cells develop and result in a regular distribution of cusps on the liquid/solid phase change interface. The predicted phenomena are consistent with the published experimental results of ref. [6]. With the increase of the melt depth the size of the convection cells increases and the number of cells decreases. At $Fo = 0.173$ two major large circulation cells exist. With further increase of the melt depth the size of the left cell increases and that of the right cell decreases. Because of the asymmetric distribution of the convection cells the phase change interface is also asymmetric although the container geometry and boundary condition are symmetric. Predictions of the asymmetric flow patterns and phase change interface are in accord with the experimental results of ref. [6].

Corresponding to the flow patterns in Fig. 7, Figs. 8a and 8b present the local dimensionless heat flux distributions. Figure 8a shows that the dimensionless heat flux distribution at $Fo = 0.0864$ is wave-like corresponding to the multiple convection cells of Fig. 7-a1. There are four crests and three troughs on the dimensionless heat flux curve of $Fo = 0.0864$ displayed in Fig. 8a. These crests and troughs correspond to the seven junctions of the eight convection cells in the streamlines shown in Fig. 7-a1. The first crest from left corresponds to the junction of the first and second convection cells. The flow direction of the first circulation is clockwise and the second circulation is anticlockwise. The liquid layers from the two circulation

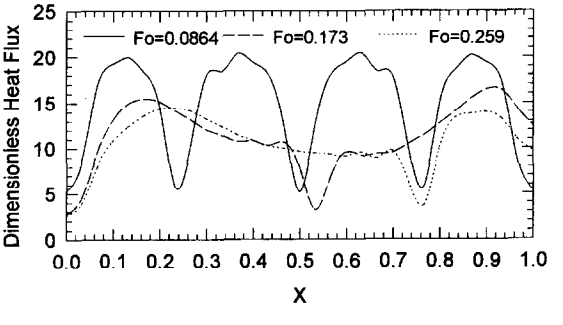

(a) *Fo=0.0864, 0.173, 0.259*

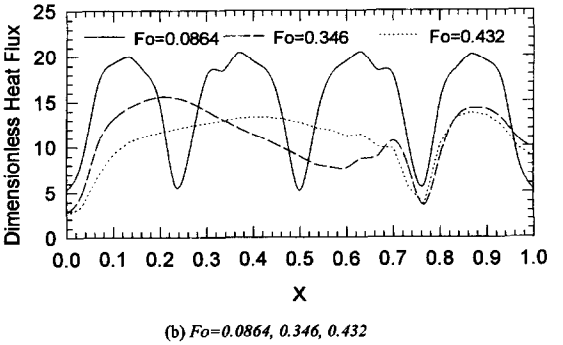

(b) *Fo=0.0864, 0.346, 0.432*

Fig. 8. Local dimensionless heat flux distribution along the heated surface at different Fo values ($Ra = 2.844 \times 10^6$).

cells are cooled after passing the phase change interface and then reach the junction of the two circulation zones at the bottom. This causes a low temperature zone to develop near the junction at the bottom surface of the container. The low temperature zone is seen in the isotherms in Fig. 7-b1. Since the bottom surface of the container is isothermal, a low temperature near the bottom isothermal surface means a large temperature difference for heat transfer. This results in higher heat flux.

The first trough from left corresponds to the junction of the second and the third convection cells in Fig. 7-a1. Since the flow direction of the second circulation is anti-clockwise and the third circulation is clockwise, at the junction of the two cells a high temperature zone is developed. This is shown in the corresponding isotherms in Fig. 7-b1. A higher temperature near the bottom isothermal surface results in a lower temperature difference for heat transfer from the wall. The lower temperature difference results in a reduced heat flux. Similar explanation applies to the other crests and troughs in the dimensionless heat flux distributions.

The heat flux distribution curve at $Fo = 0.0173$ in Fig. 8a shows that the heat flux close to the left vertical wall is very low although the flow direction of the first large convection cell from left is anti-clockwise in Fig. 7-a2. This is caused by the small circulation bubble in the bottom-left corner. This bubble results in a high temperature zone. The high temperature zone leads to a reduced heat flux along the bottom isothermal surface. Similarly, the trough on the heat flux curve corresponds to the junction of the two large convection cells seen in Fig. 7-a2.

Figure 9 shows the predicted streamlines and isotherms at different Fo values for $Ra = 2.844 \times 10^7$. From these figures it is observed that the flow patterns at this Rayleigh number are quite irregular. The flow is not symmetric and is varying with time in the melting process. Because of the asymmetry of the flow pattern the phase change interface is also asymmetric.

Corresponding to the streamlines in Fig. 9, Fig. 10 displays the local dimensionless heat flux distributions. Due to the irregularity of the flow patterns the heat flux distribution is also quite irregular and complex.

A comparison of the streamline pictures at different Rayleigh numbers shows that the flow patterns are completely different at different Rayleigh numbers. At high Rayleigh numbers the flow patterns are always varying with the melting process. At low Rayleigh numbers the flow patterns and phase change interfaces are symmetric due to the symmetry of the boundary condition. However, the flow patterns are asymmetric at high Rayleigh numbers although the boundary condition is symmetric. Due to the asymmetry of the flow patterns the phase change interface is also asymmetric. This phenomena was observed in the experiment of ref. [6].

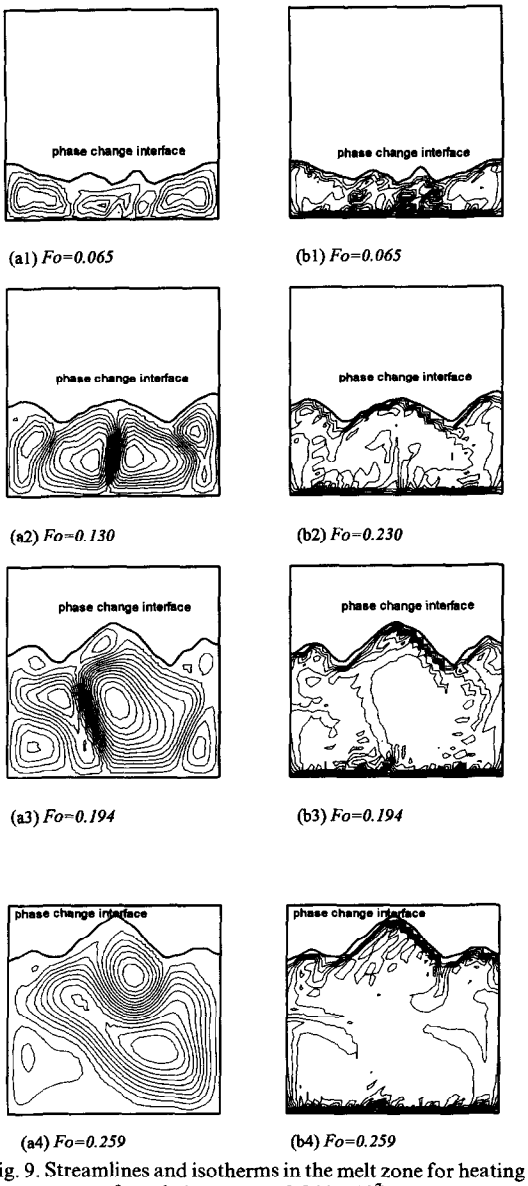

Fig. 9. Streamlines and isotherms in the melt zone for heating from below ($Ra = 2.844 \times 10^7$).

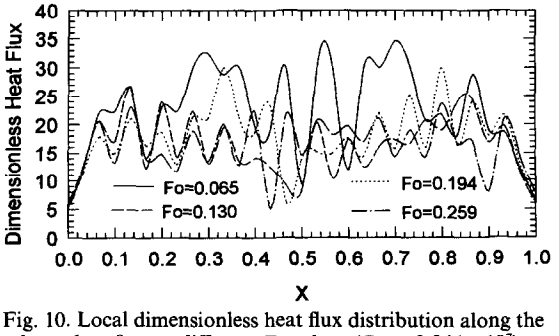

Fig. 10. Local dimensionless heat flux distribution along the heated surface at different Fo values ($Ra = 2.844 \times 10^7$).

6. CONCLUDING REMARKS

Melting of a phase change material in a rectangular cavity heated from below is simulated using a finite element model. Different flow patterns are obtained at different Rayleigh numbers. Complex and time-dependent flow patterns are obtained at high Rayleigh numbers. The obtained flow patterns are qualitatively consistent with published results.

REFERENCES

1. Yen, Y. C. and Galea, F., Onset of convection in a layer of water formed by melting of ice from below. *Physics of Fluid*, 1968, **11**, 1263–1269.
2. Yen, Y. C., Free convection heat transfer characteristics in a melt water layer. *Journal of Heat Transfer*, 1980, **103**, 550–556.
3. Seki, N., Fukosako, S. and Sugawara, M., A criteria on onset of free convection in a horizontal melted water layer with free surface. *Transactions of ASME Series C, Journal of Heat Transfer*, 1977, **99**, 92–98.
4. Hale, N. W. and Viskanta, R., Solid–liquid phase change heat transfer and interface motion in materials cooled or heated from above or below. *International Journal of Heat and Mass Transfer*, 1980, **23**, 283–292.
5. Gau, C., Viskanta, R. and Ho, C. J., Flow visualization during solid–liquid phase change heat transfer II. Melting in a rectangular cavity. *Int. Comm. Heat Mass Transfer*, 1983, **10**, 183–190.
6. Díaz, L. A. and Viskanta, R., Visualization of the solid–liquid interface morphology formed by natural convection during melting of a solid from below. *Int. Comm. Heat Mass Transfer*, 1984, **11**, 35–43.
7. Voller, V. R. and Prakash, C., A fixed grid numerical modelling methodology for convection–diffusion mushy region phase-change problems. *International Journal of Heat and Mass Transfer*, 1987, **30**, 1709–1719.
8. Brent, A. D., Voller, V. R. and Reid, K. J., Enthalpy–porosity technique for modelling convection–diffusion phase change : application to the melting of a pure metal. *Numerical Heat Transfer*, 1988, **13**, 297–318.
9. Hughes, T. J. R., Liu, W. K. and Brooks, A., Review of finite element analysis of incompressible viscous flows by the penalty function formulation. *Journal of Computational Physics*, 1979, **30**, 1–60.
10. Brooks, A. N. and Hughes, T. J. R., Streamline upwind/Petrov–Galerkin formulations for convection dominated flows with particular emphasis on the incompressible Navier–Stokes equations. *Comp. Meth. Appl. Mech. Eng.*, 1982, **32**, 199–259.
11. Heinrich, J. C. and Yu, C. C., Finite element simulation of buoyancy-driven flows with emphasis on natural convection in a horizontal circular cylinder. *Comp. Meth. Appl. Mech. Eng.*, 1988, **69**, 1–27.
12. Argyris, J., Petrov–Galerkin finite element approach to coupled heat and fluid flow. *Comp. Meth. Appl. Mech. Eng.*, 1992, **94**, 181–200.
13. Voller, V. R., Fast implicit finite-difference method for the analysis of phase change problems. *Numerical Heat Transfer*, 1990, **17**, 155–169.
14. Swaminathan, C. R. and Voller, V. R., On the enthalpy method. *Int. Num. Meth. Heat Fluid Flow*, 1993, **3**, 233–244.
15. Gong, Z. X. and Mujumdar, A. S., A finite element model for convection-dominated melting and solidification problems. *Int. J. Num Meth. Heat Fluid Flow*, accepted.
16. Gau, C. and Viskanta, R., Melting and solidification of pure metal on a vertical wall. *Journal of Heat Transfer*, 1986, **174**, 174–181.
17. Lacroix, M., Predictions of natural-convection-dominated phase-change problems by the vorticity–velocity formulation of the Navier–Stokes equations. *Numerical Heat Transfer*, Part B, 1992, **22**, 79–93.